A Near-infrared-faint, Far-infrared-luminous Dusty Galaxy at z 5 in COSMOS-Web

Jed Mckinney, Sinclaire M. Manning, Olivia R. Cooper, Arianna S. Long, Hollis Akins, Caitlin M. Casey, Andreas L. Faisst, Maximilien Franco, Christopher C. Hayward, Erini Lambrides, et al.

The Astrophysical Journal, 956:72 (12pp), 2023 October 20 https://doi.org/10.3847/1538-4357/acf614

A Near-infrared-faint, Far-infrared-luminous Dusty Galaxy at $z \sim 5$ in COSMOS-Web

Jed McKinney[1], Sinclaire M. Manning[2,26], Olivia R. Cooper[1,27], Arianna S. Long[1,26], Hollis Akins[1], Caitlin M. Casey[1], Andreas L. Faisst[3], Maximilien Franco[1], Christopher C. Hayward[4], Erini Lambrides[5,28], Georgios Magdis[6,7,8], Katherine E. Whitaker[2,6], Min Yun[2], Jaclyn B. Champagne[9], Nicole E. Drakos[10], Fabrizio Gentile[11,12], Steven Gillman[6,7], Ghassem Gozaliasl[13,14], Olivier Ilbert[15], Shuowen Jin[6,7], Anton M. Koekemoer[16], Vasily Kokorev[17], Daizhong Liu[18], R. Michael Rich[19], Brant E. Robertson[10], Francesco Valentino[6,8], John R. Weaver[20], Jorge A. Zavala[21], Natalie Allen[6,8], Jeyhan S. Kartaltepe[22], Henry Joy McCracken[23], Louise Paquereau[23], Jason Rhodes[24], Marko Shuntov[25], and Sune Toft[6,8]

[1] Department of Astronomy, The University of Texas at Austin, Austin, TX, USA
[2] Department of Astronomy, University of Massachusetts Amherst, 710 N Pleasant Street, Amherst, MA 01003, USA
[3] Caltech/IPAC, MS 314-6, 1200 E. California Blvd. Pasadena, CA 91125, USA
[4] Center for Computational Astrophysics, Flatiron Institute, 162 Fifth Avenue, New York, NY 10010, USA
[5] NASA-Goddard Space Flight Center, Code 662, Greenbelt, MD, 20771, USA
[6] Cosmic Dawn Center (DAWN), Copenhagen, Denmark
[7] DTU-Space, Technical University of Denmark, Elektrovej 327, DK-2800 Kgs. Lyngby, Denmark
[8] Niels Bohr Institute, University of Copenhagen, Jagtvej 128, DK-2200, Copenhagen, Denmark
[9] Steward Observatory, University of Arizona, 933 N. Cherry Avenue, Tucson, AZ 85719, USA
[10] Department of Astronomy and Astrophysics, University of California, Santa Cruz, 1156 High Street, Santa Cruz, CA 95064, USA
[11] University of Bologna - Department of Physics and Astronomy "Augusto Righi" (DIFA), Via Gobetti 93/2, I-40129 Bologna, Italy
[12] INAF- Osservatorio di Astrofisica e Scienza dello Spazio, Via Gobetti 93/3, I-40129, Bologna, Italy
[13] Department of Computer Science, Aalto University, PO Box 15400, Espoo, FI-00 076, Finland
[14] Department of Physics, Faculty of Science, University of Helsinki, FI-00014 Helsinki, Finland
[15] Aix Marseille Univ, CNRS, CNES, LAM, Marseille, France
[16] Space Telescope Science Institute, 3700 San Martin Drive, Baltimore, MD 21218, USA
[17] Kapteyn Astronomical Institute, University of Groningen, PO Box 800, 9700 AV Groningen, The Netherlands
[18] Max-Planck-Institut für Extraterrestrische Physik (MPE), Giessenbachstr. 1, D-85748 Garching, Germany
[19] Department of Physics and Astronomy, UCLA, PAB 430 Portola Plaza, Box 951547, Los Angeles, CA 90095-1547, USA
[20] Department of Astronomy, University of Massachusetts, Amherst, MA 01003, USA
[21] National Astronomical Observatory of Japan, 2-21-1 Osawa, Mitaka, Tokyo 181-8588, Japan
[22] Laboratory for Multiwavelength Astrophysics, School of Physics and Astronomy, Rochester Institute of Technology, 84 Lomb Memorial Drive, Rochester, NY 14623, USA
[23] Institut d'Astrophysique de Paris, UMR 7095, CNRS, and Sorbonne Université, 98bis Boulevard Arago, F-75014 Paris, France
[24] Jet Propulsion Laboratory, California Institute of Technology, 4800 Oak Grove Drive, Pasadena, CA 91001, USA
[25] Institut d'Astrophysique de Paris, CNRS, Sorbonne Université, 98bis Boulevard Arago, F-75014, Paris, France
Received 2023 April 13; revised 2023 August 21; accepted 2023 August 31; published 2023 October 10

Abstract

A growing number of far-infrared (FIR) bright sources completely invisible in deep extragalactic optical surveys hint at an elusive population of $z > 4$ dusty, star-forming galaxies. Cycle 1 JWST surveys are now detecting their rest-frame optical light, which provides key insight into their stellar properties and statistical constraints on the population as a whole. This work presents the JWST Near Infrared Camera (NIRCam) counterpart from the COSMOS-Web survey to an FIR SCUBA-2 and Atacama Large Millimeter/submillimeter Array (ALMA) source, AzTECC71, which was previously undetected at wavelengths shorter than 850 μm. AzTECC71, among the reddest galaxies in COSMOS-Web with F277W − F444W ~ 0.9, is undetected in NIRCam/F150W and F115W and fainter in F444W than other submillimeter galaxies identified in COSMOS-Web by 2–4 magnitudes. This is consistent with the system having both a lower stellar mass and higher redshift than the median dusty, star-forming galaxy. With deep ground- and space-based upper limits combined with detections in F277W, F444W, and the FIR including ALMA Band 6, we find a high probability (99%) that AzTECC71 is at $z > 4$ with $z_{\rm phot} = 5.7^{+0.8}_{-0.7}$. This galaxy is massive ($\log M_*/M_\odot \sim 10.7$) and infrared-luminous ($\log L_{\rm IR}/L_\odot \sim 12.7$), comparable to other optically undetected but FIR-bright dusty, star-forming galaxies at $z > 4$. This population of luminous, infrared galaxies at $z > 4$ is largely unconstrained but comprises an important bridge between the most extreme dust-obscured galaxies and more typical high-redshift star-forming galaxies. If further FIR-selected galaxies that drop out of the F150W filter in COSMOS-Web have redshifts $z > 4$ like AzTECC71, then the volume density of such sources may be $\sim$3–10 $\times$ greater than previously estimated.

[26] NASA Hubble Fellow.
[27] NSF Graduate Research Fellow.
[28] NPP Fellow.

Unified Astronomy Thesaurus concepts: Far infrared astronomy (529); High-redshift galaxies (734); Ultraluminous infrared galaxies (1735); Galaxy evolution (594)

1. Introduction

"Submillimeter galaxies" (SMGs; $S_{850} \gtrsim 1$ mJy) are sources selected from blind surveys made with single-dish telescopes operating at submillimeter wavelengths, such as SCUBA-2 on the James Clerk Maxwell Telescope (JCMT; Holland et al. 2013; Casey et al. 2013; Chen et al. 2013). These SMGs are typically massive ($M_*/M_\odot \sim 10^{11}$) and infrared-luminous ($L_{\rm IR} > 10^{12}$) with an average redshift of $z \sim 2.5$ (see, e.g., Casey et al. 2014; Hodge & da Cunha 2020). SMGs play an important role within the framework of galaxy evolution as the most prolific star factories in the Universe whose number counts and properties challenge theoretical models (e.g., Murphy et al. 2011; Casey et al. 2014).

Given its sensitivity and spatial resolution, the Atacama Large Millimeter/submillimeter Array (ALMA) has revealed a subset of the broader SMG population with $z > 3$–4 (Simpson et al. 2014; Danielson et al. 2017; Koprowski et al. 2017; Dudzevičiūtė et al. 2020; Shu et al. 2022). These galaxies make up ∼20%–30% of all SMGs and can be undetected in deep optical surveys (Wardlow et al. 2011; Casey et al. 2014; Simpson et al. 2014; Franco et al. 2018). In fact, infrared-bright galaxies have eluded optical detection since the first blind surveys at submillimeter (mm) wavelengths. For example, uncovering the optical counterpart to the first source ever discovered in an unbiased extragalactic survey at 850 μm, HDF850.1 (Hughes et al. 1998), spanned a 16 yr long debate (e.g., Dunlop et al. 2004; Cowie et al. 2009; Walter et al. 2012; Serjeant & Marchetti 2014). The optically faint nature of typical SMGs arises from extreme dust extinction (e.g., da Cunha et al. 2015), whereas optically undetected ("dark") SMGs have equal or greater attenuation and higher redshifts on average (e.g., Franco et al. 2018, 2020; Smail et al. 2021; Shu et al. 2022). Importantly, as reviewed by Long et al. (2023), the number count estimates of such sources above $z > 4$ exhibit over 2 orders of magnitude in dispersion due to differences in survey area and wavelength coverage. These factors produce drastically different levels of completeness in stellar mass, redshift, and volume.

Accurate measurements of the number densities of $z > 3$–4 SMGs, their physical properties, and their contributions to the cosmic star formation rate density have been largely unconstrained, which may substantially alter our view of early star formation based on UV-bright Lyman-break galaxies (e.g., Madau & Dickinson 2014; Novak et al. 2017; Liu et al. 2018; Gruppioni et al. 2020; Zavala et al. 2021; Algera et al. 2023).

While faint or undetected optical/near-infrared (NIR) photometry makes measuring stellar properties difficult in SMGs, the limiting submillimeter spatial resolution poses an equal challenge in terms of counterpart identification. SCUBA-2 has been a powerful instrument for surveying wide fields in the submillimeter (e.g., Casey et al. 2014), but its ∼11″ resolution (∼70 kpc at $z = 4$–5) at 850 μm on the JCMT allows for many possible optical counterparts within a given submillimeter source (e.g., Jin et al. 2018; Liu et al. 2018). ALMA and/or deep Very Large Array (VLA) imaging at high spatial resolution is critical for assigning far-infrared (FIR) emission to optical/NIR counterparts (e.g., Simpson et al. 2015; Zavala et al. 2018). Working toward a better census on the optically faint/dark $z > 3$–4 SMG population in the era of JWST extragalactic fields, we present our analysis on the selection of optically faint FIR-bright SMGs and comment on the nature of one exceptional source at $z > 4$ with no prior non-JWST counterpart below $\lambda_{\rm obs} = 850$ μm. Large-area and deep JWST surveys such as COSMOS-Web (Casey et al. 2023) will have the potential to uncover many of these optically faint/dark SMGs at $z \gtrsim 3$–4 and allow us to study their redshift distribution and physical properties.

In this paper we present the JWST/NIRCam detection of AzTECC71, a known FIR/submillimeter-only source (Brisbin et al. 2017; Simpson et al. 2019). We discuss the multi-wavelength associations and photometry in Section 2, and spectral energy distribution fits to the data in Section 3. In Section 4 we discuss the nature of this source and implications for $4 < z < 6$ star-forming galaxy volume densities. Section 5 summarizes the main conclusions. Throughout this work we adopt a ΛCDM cosmology with $\Omega_m = 0.3$, $\Omega_\Lambda = 0.7$, and $H_0 = 70\,{\rm km\,s^{-1}\,Mpc^{-1}}$. We use a Chabrier initial mass function (IMF).

2. Data and Selection

2.1. Searching for Near-infrared Counterparts to Submillimeter Sources in COSMOS-Web

Large-area JWST surveys are well-suited to uncovering the rest-frame optical emission originating from the intrinsically rare population of high-redshift dusty, star-forming galaxies that are FIR/submillimeter-bright (Casey et al. 2014; Hodge & da Cunha 2020). In this work, we search for ALMA counterparts to SCUBA-2 850 μm sources with signal-to-noise ratios (S/Ns) greater than 4 from S2COSMOS (Simpson et al. 2019) within the COSMOS-Web 2023 January mosaic (M. Franco et al. 2023, in preparation; Casey et al. 2023). Upon completion, COSMOS-Web will map a contiguous 0.54 deg^2 area within the Cosmic Evolution Survey (COSMOS; Scoville et al. 2007) in four JWST/NIRCam bands (F115W, F150W, F277W, F444W) and a noncontiguous 0.19 deg^2 area in Mid-Infrared Instrument (MIRI) F770W. The 2023 January data include six visits covering just 4% (77.76 arcmin^2) of the total COSMOS-Web area.

The data reduction of COSMOS-Web will be described in full in M. Franco et al. (2023, in preparation) In summary, we reduce the JWST/NIRCam data with the JWST Calibration Pipeline version 1.8.3 with modifications for background and $1/f$ noise subtraction following other JWST extragalactic programs (e.g., Bagley et al. 2023; Finkelstein et al. 2023). We use version 0989 of the Calibration Reference Data System.[29] The final mosaics have a resolution of 0.″03 pixel^{-1} and have been aligned to COSMOS2020, which in turn has been aligned to Gaia Early Data Release 3 (Weaver et al. 2022). See Casey et al. (2023) for 5σ depths in each of the four COSMOS-Web NIRCam filters.

FIR interferometric observations of the dust continuum emission are critical for a robust optical/NIR counterpart identification to the low-resolution submillimeter SCUBA-2 data. The JWST counterparts and general properties of a larger

[29] jwst-crds.stsci.edu

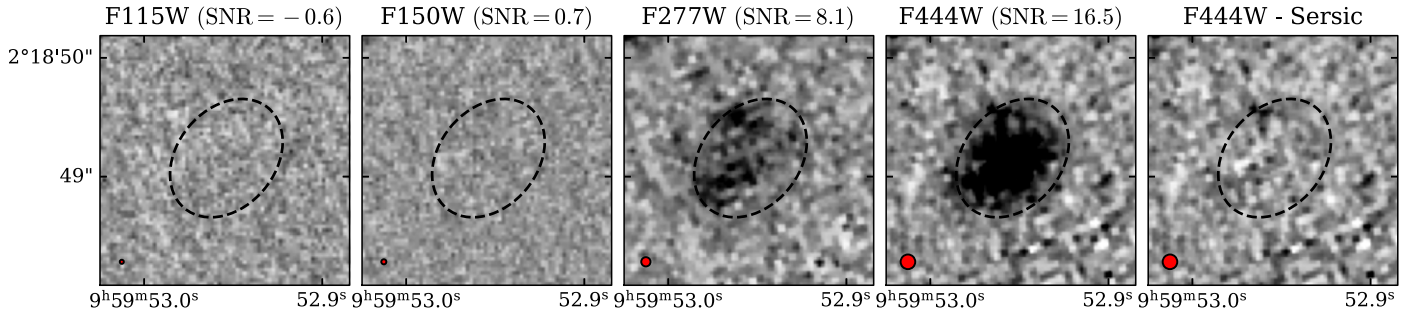

Figure 1. 2″ × 2″ JWST/NIRCam cutouts from COSMOS-Web (M. Franco et al. 2023, in preparation; Casey et al. 2023) of AzTECC71. On each panel we show the elliptical aperture fit to the F444W detection (black dashed ellipse). The rightmost panel shows the residual between the F444W detection and a PSF-convolved 2D Sersic profile with $r_{1/2} = 0\farcs32$ and $n_{\rm sersic} = 0.74$. Red circles denote the PSF for each band shown. The S/Ns of the flux densities extracted through the elliptical aperture are listed above each panel.

ALMA/submillimeter-selected sample from COSMOS-Web will be discussed in a future work (S. Manning et al., in preparation). In this study we present the analysis of the faintest NIRCam/F444W submillimeter source in our catalog, AzTECC71.

AzTECC71 was originally detected at 1.1 and 1.2 mm in the AzTEC/ASTE and MAMBO/IRAM 30 m maps of the COSMOS field but its redshift was unknown due to the lack of detections in the optical (Bertoldi et al. 2007; Aretxaga et al. 2011). It is detected at 850 μm by SCUBA-2 (Simpson et al. 2019), but not at 450 μm (e.g., Casey et al. 2013; Geach et al. 2017; Lim et al. 2020). Brisbin et al. (2017) conducted an ALMA Band 6 (1250 μm) follow-up survey of bright SCUBA-2 sources in COSMOS, and reported a 6.3σ detection for AzTECC71 at R.A., decl. = $9^{\rm h}59^{\rm m}52\fs95$, $2^{\rm d}18^{\rm m}49\fs13$ from program 2013.1.00118.S (PI: M. Aravena), coincident with a NIRCam/F444W source in COSMOS-Web. Prior to the identification of its NIRCam/F444W counterpart AzTECC71 had no reported >5σ detection below 850 μm including data from the Hubble Space Telescope (HST) and Spitzer. As there are no other optical/NIR counterparts within 1″ of the ALMA detection, AzTECC71 is not in the COSMOS2020 catalog (Weaver et al. 2022). AzTECC71 will not be covered by COSMOS-Web's MIRI mosaic.

Figure 1 shows AzTECC71's JWST/NIRCam counterpart from COSMOS-Web (M. Franco et al. 2023, in preparation; Casey et al. 2023). The galaxy is detected in F277W and F444W but shows no detection in NIRCam's F115W and F150W bands with respective depths of 27.45 and 27.66 AB magnitudes. From a point spread function (PSF)-convolved 2D Sersic surface brightness profile fit to the F444W map (Figure 1, *right*), AzTECC71 has a half-light radius ($r_{1/2}$) of $0\farcs32 \pm 0\farcs01$ at 4.44 μm, and a Sersic index ($n_{\rm sersic}$) of 0.74 ± 0.02. Errors on $r_{1/2}$ and $n_{\rm sersic}$ are bootstrapped from 1000 perturbations of the F444W map with noise drawn from the background pixel flux distribution within 4″ of AzTECC71. We use the strong F444W detection to refine upper limits from the ground- and space-based imaging data, as described in the next section.

2.2. Optical/Near-infrared Photometry

AzTECC71 shows an extended F444W morphology (Figure 1). Therefore, we measure photometry and upper limits using an elliptical aperture constructed to match the source morphology in F444W with a semimajor axis of $a = 0\farcs55$, an axis ratio of $b/a = 0.75$, and a position angle of $\phi = 40°$ N of W. The semimajor/minor axes are greater than $r_{1/2}$ from the 2D Sersic fits and encase the extent of pixels >5σ in the F444W map (Figure 1). We sum all pixels within the ellipse when calculating the flux densities and emphasize that this is not model-based photometry. AzTECC71 is detected at a S/N of 16.5 in F444W ($m_{\rm F444W,AB} = 24.62$) and 8.1 in F277W ($m_{\rm F277W,AB} = 25.51$). The galaxy is not detected in either of the other COSMOS-Web JWST/NIRCam bands (F115W, F150W) nor any other optical/NIR imaging in COSMOS. We calculate upper limits from these nondetections by summing the corresponding pixels within the elliptical aperture. Then we apply aperture corrections to account for PSF variations by computing the fraction of each lower-resolution PSF that falls outside of our elliptical aperture shown in Figure 1. This is most relevant for the ground-based data in which the source would be unresolved. For the ground-based data, we adopt the PSFs used in the COSMOS2020 catalog (Weaver et al. 2022). The aperture correction to lower-resolution ground-based imaging ranges from 2.1 to 2.4, and is 1.1 for HST Advanced Camera for Surveys (ACS; Koekemoer et al. 2007). Additionally, using our refined aperture we recover a 3σ detection by the Infrared Array Camera (IRAC; 4.5 μm) where no detection was previously reported for lack of an optical/NIR counterpart. JWST/NIRCam and updated flux densities and limits are listed in Table 1.

2.3. Infrared through Radio Data

AzTECC71 is detected at 850 μm (SCUBA-2/JCMT; Simpson et al. 2019), 1100 μm (AzTEC; Aretxaga et al. 2011), 1200 μm (MAMBO; Bertoldi et al. 2007), and 1250 μm (ALMA B6; Brisbin et al. 2017), where the peak pixel flux within the elliptical aperture fit to the F444W map is >5 × the map noise. In the case of the ALMA Band 6 detection, we restore AzTECC71's calibrated visibilities from Project 2013.1.00118.S (PI: Aravena) hosted in the ALMA archive. We image the data with `tclean` and naturally weighted visibilities. The source is not spatially resolved by the $1\farcs55 \times 0\farcs92$ synthesized beam, so the naturally weighted image maximizes the S/N. We then calculate the peak flux density from the primary-beam-corrected image, listed in Table 1. We estimate the maximum size of the source in the Band 6 data from Equation (1) in Martí-Vidal et al. (2014), which limits the size to <0.″44 (consistent with the F444W radius; see Section 2.1). The ALMA Band 6 continuum detection is shown over an RGB image constructed from the NIRCam bands in Figure 2.

Table 1
AzTECC71 Multiwavelength Photometry

Band	λ_c	Unit	Flux
CFHT-*u*	375 nm	nJy	(-14.1 ± 9.1)
HSC-*g*	476 nm	nJy	(-2.9 ± 10.2)
HSC-*r*	617 nm	nJy	(4.5 ± 17.1)
HSC-*i*	768 nm	nJy	(13.1 ± 29.6)
ACS/F814W	814 nm	nJy	(2.0 ± 7.6)
HSC-*z*	891 nm	nJy	(28.1 ± 26.8)
HSC-*y*	976 nm	nJy	(-18.0 ± 55.2)
UVISTA Y	1.02 μm	μJy	(0.11 ± 0.11)
UVISTA J	1.25 μm	μJy	(0.17 ± 0.14)
UVISTA H	1.63 μm	μJy	(0.14 ± 0.16)
UVISTA Ks	2.14 μm	μJy	(0.16 ± 0.12)
NIRCam/F115W	1.15 μm	nJy	(-31 ± 51)
NIRCam/F150W	1.50 μm	nJy	(33 ± 50)
NIRCam/F277W	2.77 μm	nJy	227 ± 28
NIRCam/F444W	4.44 μm	nJy	513 ± 31
IRAC/Ch1	3.6 μm	nJy	(508 ± 274)
IRAC/Ch2	4.5 μm	nJy	706 ± 228
IRAC/Ch3	5.8 μm	μJy	(1.6 ± 0.30)
IRAC/Ch4	8.0 μm	μJy	(1.8 ± 0.41)
MIPS[a]	24 μm	μJy	(-0.22 ± 18)
PACS[b]	100 μm	mJy	(-0.01 ± 1.5)
PACS[b]	160 μm	mJy	(0.13 ± 2.9)
SPIRE	250 μm	mJy	(14.5 ± 5.8)
SPIRE	350 μm	mJy	(28.5 ± 6.3)
SCUBA-2	450 μm	mJy	(4.0 ± 6.1)
SPIRE	500 μm	mJy	(27.2 ± 6.1)
SCUBA-2	850 μm	mJy	4.31 ± 0.78
AzTEC[c]	1100 μm	mJy	2.4 ± 1.1
MAMBO[d]	1200 μm	mJy	3.1 ± 1.3
ALMA/B6	1250 μm	mJy	2.16 ± 0.20
ALMA/B4	2 mm	mJy	(0.30 ± 0.23)
VLA/3 GHz	10 cm	μJy	(3.2 ± 2.3)

Notes. Flux densities reported in parentheses correspond to limits on the SED as discussed in Section 2. In general, we report pixel values at the ALMA/B6 position and their 1σ uncertainties.
[a] Le Floc'h et al. (2009).
[b] Lutz et al. (2011).
[c] Aretxaga et al. (2011).
[d] Bertoldi et al. (2007).

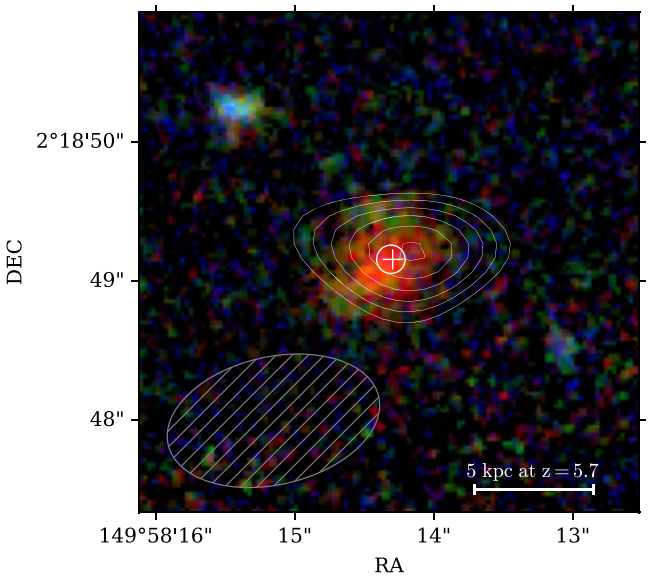

Figure 2. $3\farcs6 \times 3\farcs6$ RGB image constructed from R = F444W, G = F277W, B = (F115W+F150W stack). White contours are ALMA Band 6 continuum at 1250 μm drawn at 5 through 10σ in increments of 1σ. The source is not spatially resolved by ALMA. The white circle corresponds to the centroid of the F444W image. The white + is the centroid of a 2D Gaussian fit to the ALMA detection.

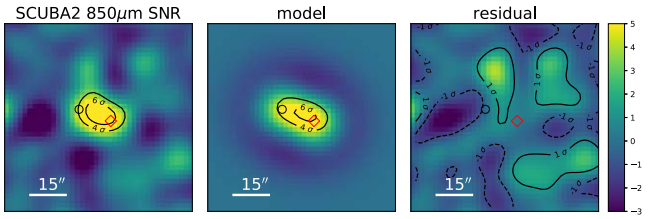

Figure 3. $80'' \times 80''$ cutout of the SCUBA-2 S/N map (left) illustrating the deblending of the SCUBA-2 850 μm flux using ALMA Band 6 positional priors for AzTECC71 (red diamond) and the nearby $z = 0.829$ dusty galaxy (black circle). The model based on two scaled point sources fixed to the Band 6 positions is shown in the middle panel, with the residual shown in the far right.

Two submillimeter sources are detected in the ALMA/B6 imaging of AzTECC71 at S/N > 5, one coincident with the JWST/NIRCam imaging and another $15''$ away with a spectroscopic redshift of $z_s = 0.829$ (AzTECC71b; Brisbin et al. 2017). Both sources contribute to blended submillimeter flux measured by the single-dish facilities, as is common for 10%–20% of all submillimeter galaxies (SMGs; $S_{850\mu m} > 1$ mJy; Chen et al. 2013; Hayward et al. 2013, 2018; Koprowski et al. 2014; Michałowski et al. 2017). The ALMA map provides secure positional priors for the origin of the submillimeter emission from each galaxy, so we deblend the SCUBA-2 flux densities by fitting point-source models fixed to the positions of each ALMA source. We use the SCUBA-2 PSF from Simpson et al. (2017). The results are shown in Figure 3 with the updated flux density for AzTECC71 listed in Table 1 at an S/N of 5.5. The relative contribution of AzTECC71 to the total blended SCUBA-2 flux density is 55^{+1}_{-3}%. The FIR data at $\lambda_{obs} > 850$ μm are beyond the spectral energy distribution (SED) peak for both AzTECC71 and the submillimeter source at $z = 0.829$ so we scale AzTECC71's AzTEC ($34''$ resolution) and MAMBO ($11''$ resolution) fluxes by this same factor. We do not apply this to the blended Herschel data, which cover the SED peak of both sources, where differences in dust temperatures between the two will change the relative band-to-band scaling.

In the case of nondetections in the mid-IR and FIR, we set the flux density to that of the pixel containing our target and adopt the rms derived for the total mosaic as the 1σ uncertainty. In the case of Herschel Spectral and Photometric Imaging REceiver (SPIRE), this uncertainty corresponds to the confusion limit. We thereby constrain the flux/uncertainty at 24 μm (Spitzer/MIPS; Le Floc'h et al. 2009), 100–500 μm (Herschel/PACS+SPIRE; Lutz et al. 2011; Oliver et al. 2012), 450 μm (SCUBA-2; Casey et al. 2013), 2 mm (ALMA/B4; A. Long 2023, in preparation; Casey et al. 2021), and 3 GHz (VLA; Smolčić et al. 2017) using the corresponding imaging data in the COSMOS field. For the Herschel/SPIRE bands, this gives the appearance of a detection (Table 1); however, the SPIRE data at the position of AzTECC71 are likely blended with neighboring sources as is common in confusion-limited SPIRE maps and as expected based on the submillimeter blending. Thus, the overlapping pixel contains some mix of emissions from AzTECC71 and its neighbors. We test deblending the

Herschel maps following the method outlined previously for the SCUBA-2 data, but this is highly uncertain because of the larger Herschel PSFs and higher confusion noise limits ($\sigma_{\rm conf}$). Our attempts at Herschel deblending yield fluxes below the confusion limit for AzTECC71 and thus do not adequately constrain the source emission. Rather, by using the pixel flux at the position of the source $\pm\sigma_{\rm conf}$ we take a conservative approach and allow the SED fits to marginalize over the uncertainty in the flux association with AzTECC71 and its neighbors for the blended SPIRE photometry.

3. Spectral Energy Distribution Fits and Derived Properties

We fit the optical through radio photometry/limits listed in Table 1 with CIGALE—a multiwavelength fitting code that handles UV/optical and infrared (IR) energy balance (Boquien et al. 2019). To test the constraint from FIR data alone as may be available for many highly attenuated sources at $z \gtrsim 4$ without JWST, and to test the consistency with energy balance between UV/optical and IR, we also fit the FIR data with: MCIRSED, a Bayesian tool that fits dust emission properties (Drew & Casey 2022); and MMpz, a photometric redshift code tied solely to FIR/millimeter photometry (Casey 2020). The FIR/millimeter probability distributions are based on the measured distribution of galaxy SEDs in the empirical relation between rest-frame peak wavelength and total IR luminosity, i.e., the $L_{\rm IR}$–$\lambda_{\rm peak}$ plane described in detail in Drew & Casey (2022) and which does not evolve with the redshift. This technique accounts for intrinsic SED breadth as it probes a wide range of dust temperatures at fixed IR luminosity. Based on the FIR through submillimeter constraints alone, we estimate $z_{p,\rm MMpz} = 4.2^{+3.1}_{-1.6}$ from MMpz.

The full optical/NIR to FIR/submillimeter fit with CIGALE is critical for constraining the target's redshift and stellar mass. We fit AzTECC71 with an exponentially declining star formation history that allows for a late-stage burst with $\tau_{\rm main} = 0.1$, 1 Gyr and $\tau_{\rm burst} = 1$, 10, 100 Myr. We assume a Chabrier IMF (Chabrier 2003), a metallicity of either $Z_\odot$ or $0.2\,Z_\odot$, and a power-law dust attenuation curve $\propto\lambda^{-0.7}$ up to $A_V = 6$. We model the FIR SED as a modified blackbody with submillimeter slope $\beta \in [1.8, 3.2]$ added to a mid-IR power law with a slope $\alpha \in [1, 5]$, which accounts for a distribution in warmer dust temperatures (Casey 2012), although this regime of the SED is largely unconstrained so α is a nuisance parameter that we marginalize over. We apply a flat prior on redshift between $z = 2$–9, and the dust temperature is allowed to vary between 20 and 70 K. The wavelength corresponding to an optical depth of unity (λ_0) is fixed at 200 μm; we account for different opacity models in subsequent fits and find this assumption to have little impact on the best-fit results besides inflating uncertainties when allowed to vary. We include a power-law synchrotron component constrained by our VLA/3 GHz upper limit with a slope of 0.8 and we assume an FIR/radio correlation coefficient $q_{\rm IR} \in [1.8, 2.6]$, corresponding to the range found for massive and high-redshift star-forming galaxies (e.g., Delvecchio et al. 2021).

With MCIRSED (Drew & Casey 2022), we fit the FIR/millimeter SED to a modified blackbody added piecewise with a mid-IR power law using Bayesian analysis; best-fit SEDs are derived based on a Markov chain Monte Carlo (MCMC) convergence. The mid-IR power law is joined to the modified blackbody at the point where the blackbody slope is equal to the power-law index $\alpha_{\rm MIR} = 2$ (consistent with, e.g., Casey 2012; U et al. 2012). We allow λ_0 to vary between $\lambda_{\rm rest} = 100$–300 μm as the opacity model for high-redshift galaxies likely varies as a function of the dust geometry (e.g., Simpson et al. 2017; Jin et al. 2019, 2022a). We fix the redshift to the CIGALE best-fit photometric redshift ($z = 5.7$) and input the FIR/millimeter photometric detections and upper limits with their associated uncertainties. Given our prediction that the galaxy sits at $z \gtrsim 5$, we include a cosmic microwave background (CMB) correction term in our fitting procedure to account for ISM dust heating from the CMB at high redshift (da Cunha et al. 2013). From the MCIRSED algorithm, we find the best-fit dust SED with measurements for each of the following free parameters: emissivity spectral index (β), total IR luminosity ($L_{\rm IR}$, taken from 8 to 1000 μm), dust temperature ($T_{\rm dust}$), and rest-frame peak wavelength ($\lambda_{\rm peak}$). We marginalize over λ_0 which increases the uncertainties on $\lambda_{\rm peak}$, $T_{\rm dust}$ by 20% compared to fits fixing the opacity model to $\lambda_0 = 200$ μm.

From the SED fits we infer a photometric redshift of $z_p = 5.7^{+0.8}_{-0.7}$. Figure 4 shows the best-fit CIGALE SED at $z = 5.7$ ($\chi^2_r = 0.4$). The posterior and cumulative redshift distribution functions are shown in Figure 5 from both CIGALE and MMPz. Marginalizing over the full parameter space, the probability that the galaxy lies above $z = 4$ ($z = 5$) is 99.6% (79.0%). If we fit only the optical/NIR (OIR) SED under the same assumptions as outlined previously, we find a much broader redshift posterior consistent with the OIR+FIR/submillimeter photo $-z$ albeit with greater uncertainty: $z_{p,\rm OIR} \sim 5.7^{+1.3}_{-1.2}$. Most notably, the OIR-only SED fit allows a solution at $z \sim 2.3$ that is significantly disfavored by the FIR/submillimeter/radio data, as demonstrated in Figure 4. Interestingly, if we fit the OIR and FIR/submillimeter SED excluding JWST data, we recover a redshift posterior comparable to that of the full SED fit. This is not entirely unexpected as AzTECC71's ground- and HST-based upper limits as well as the 4.5σ IRAC4 detection leverage the NIRCam/F444W detection. Therefore the fit without JWST is not entirely representative of it is photometric redshift constraint prior to COSMOS-Web. In contrast, JWST provides an important anchor on AzTECC71's stellar mass. Figure 6 compares the stellar mass posteriors for the SED fitting cases with and without JWST. Including upper limits from NIRCam/F115W and F150W with the detections in F277W and F444W lowers the stellar mass by 0.2 dex and decreases the uncertainty by a factor of 2. The mass estimates for such high-redshift SMGs like AzTECC71 that do not have JWST counterparts could be overestimated by similar factors.

In Table 2 we list parameter estimates from the CIGALE SED fits to the optical/NIR + FIR/submillimeter/radio with uncertainties marginalizing over the χ^2 distribution. The MCIRSEDfits for T_d and $L_{\rm IR}$ to only the FIR data agree with CIGALE within 1σ. AzTECC71 is most likely a massive ($\log M_*/M_\odot \sim 10.6$) dust-obscured star-forming galaxy with $\log L_{\rm IR}/L_\odot \sim 12.6$ and SFR $\sim 800\,M_\odot\,{\rm yr}^{-1}$ at $z \sim 5.7$. This is consistent with the OIR-only SED fit, which favors a massive ($\log M_*/M_\odot \sim 10.6$), optically attenuated ($A_V \sim 3$) galaxy at $z \sim 5.7^{+1.3}_{-1.2}$. AzTECC71 must be heavily attenuated in the optical ($A_V \sim 5$) to match the red F277W/F444W color and nondetections in the NIRCam short-wavelength bands. This can be interpreted with a recent dust-obscured starburst, as is known for ultraluminous IR galaxies (ULIRGs) with $L_{\rm IR} \geqslant 10^{12}\,L_\odot$. Indeed, the dust-obscured star formation rate implied by the total IR luminosity following Kennicutt (1998)[30] is very high, $\sim 1000\,M_\odot\,{\rm yr}^{-1}$, consistent with CIGALE.

[30] ${\rm SFR_{IR}}/[M_\odot\,{\rm yr}^{-1}] = 1.8 \times 10^{-10}\,L_{\rm IR}/L_\odot$.

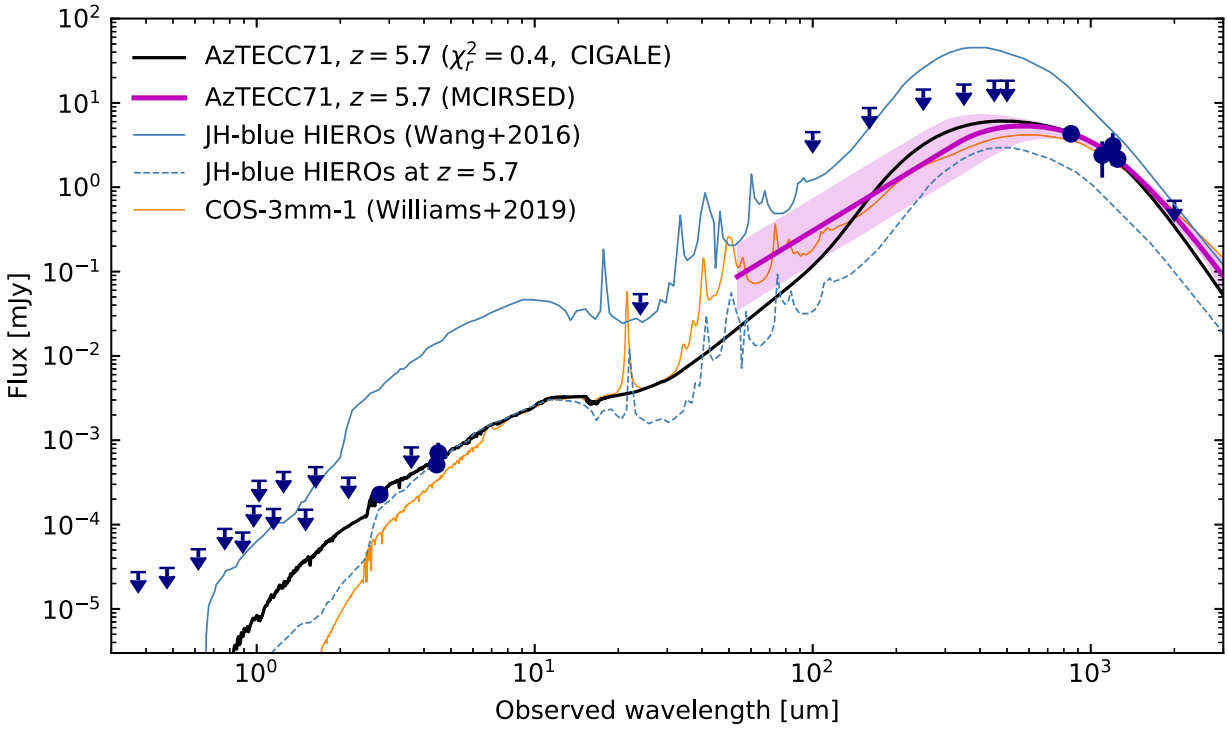

Figure 4. SED for AzTECC71. Observations are shown in blue, with circles denoting detections and arrows 3σ upper limits. The preferred $z = 5.7$ solution is shown for CIGALE with a black solid line. The optical/NIR-only fit is largely ruled out by the FIR/submillimeter data. The purple shaded region contains the uncertainty about the MCIRSED best fit (solid purple line). For comparison we show the average SED of $z > 3$ $H - [4.5]$ selected galaxies from Wang et al. (2016) in blue (solid). The best-fit SED to COS-3 mm-1, a $z \sim 5$ 3 mm selected galaxy from Williams et al. (2019) is shown in orange. AzTECC71 is fainter in the optical than $H - [4.5]$ selected massive and dusty star-forming galaxies from Wang et al. (2016), but brighter than this sample in the FIR if it were scaled to match AzTECC71 at $z = 5.7$ and 4.5 μm (blue dashed). Similar to the IR flux of COS-3 mm-1, AzTECC71 is likely part of a more IR-luminous population of massive galaxies at $z > 4$.

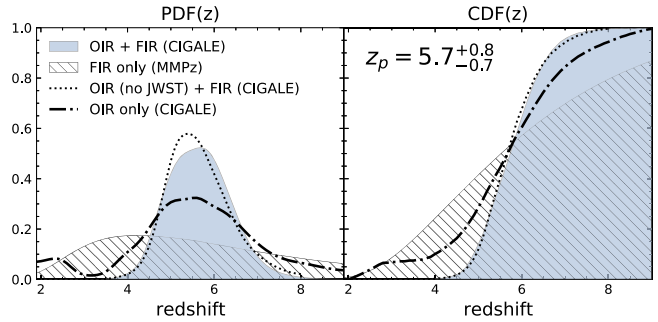

Figure 5. Posterior (left) and cumulative (right) redshift distribution function from fitting only the IR SED with MMPz (black hatched), only the optical/NIR with CIGALE (dotted–dashed), the full optical through IR SED with CIGALE (blue shaded), and a CIGALE fit excluding JWST (dotted). We report the photometric redshift (z_p) from the peak of the optical/NIR + FIR posterior distribution function and its 16th and 84th percentiles.

The MCIRSED dust SED fit favors $\lambda_{\rm peak} \sim 80\,\mu$m, corresponding to a dust temperature of $\sim 60 \pm 20$ K (see Figure 7). While MCIRSED also fits the emissivity spectral index β, this measurement is poorly constrained and is further exacerbated by the combined use of interferometric data with single-dish data that suffer from confusion boosting. Though we have accounted for deboosting and deblending as best as possible, precise measurements of β for an individual source necessitate matched-beam ALMA data at both frequencies. Taken at face value, we find $\beta = 2.7^{+0.6}_{-0.7}$, which is high compared to other estimates at $z \sim 5.5$ (e.g., Faisst et al. 2020a) but consistent with recent works that find evidence for $\beta \sim 2.4$ in $z > 4$ dusty, star-forming galaxies (Kato et al. 2018; Casey et al. 2021; Cooper et al. 2022).

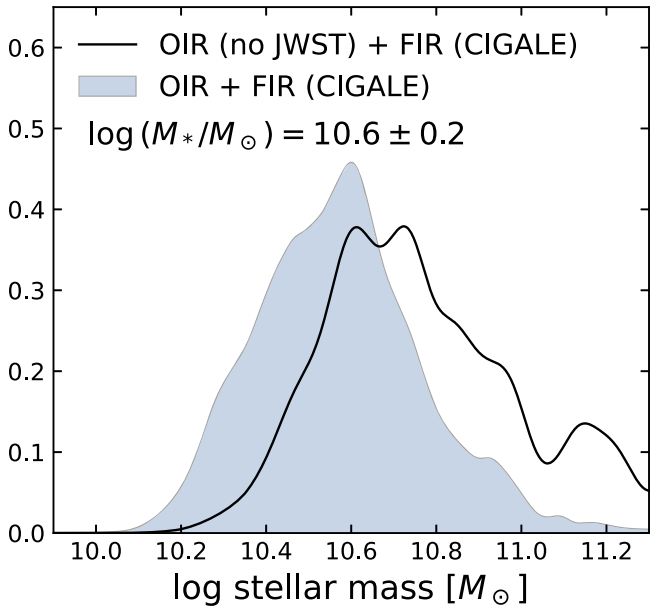

Figure 6. Stellar mass posterior distribution from the full optical through IR SED with CIGALE (blue shaded), and a CIGALE fit excluding JWST (solid line). We report the stellar mass (M_*) from the peak of the OIR + FIR CIGALE posterior and its 16th and 84th percentiles. Including JWST constraints shifts the most likely stellar mass down by $\sim$0.2 dex and lowers the uncertainty by a factor of 2.

Diagnosing the presence of an active galactic nucleus (AGN) in AzTECC71 is difficult given the lack of SED constraint in the mid-IR, a regime particularly sensitive to hot, toroidal dust emission around central supermassive black holes. At $z = 5.7$

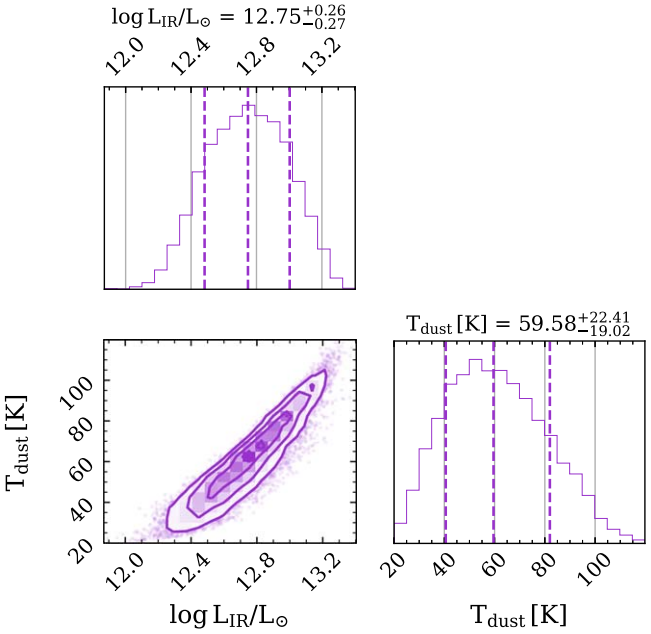

Figure 7. Corner plot showing the two-dimensional joint posterior distributions for dust SED fit parameters $L_{\rm IR}$ and $T_{\rm dust}$ derived using MCIRSED. The vertical dashed lines in the 1D histograms for each parameter show the 68% interquartile range (outer lines) and the median value (central line). The dust temperature and IR luminosity are highly covariant given the lack of rest-frame constraint straddling the dust SED peak.

and for the best-fit $\log L_{\rm IR}/L_\odot = 12.75$, our radio upper limits at 3 GHz disfavor $q_{\rm IR} < 2$ typical of radio AGN (e.g., Delvecchio et al. 2021), which would otherwise require a 3 GHz flux 3 times greater than our 3σ upper limit. However, a mid-IR spectral search for high-ionization emission lines and/or fine sampling of the mid-IR SED with JWST/MIRI would be needed to robustly rule out the presence of a heavily obscured AGN.

For the remainder of this work, we adopt stellar parameters (M_*, SFR) estimated from the full multiwavelength SED fit using CIGALE as our fiducial estimates. These are broadly consistent with both the optical-only and FIR-only fits. We adopt FIR dust parameters ($T_{\rm dust}$, $\lambda_{\rm peak}$, β, $L_{\rm IR}$) from MCIRSED, which are also consistent with CIGALE. We choose the MCIRSED numbers because this code marginalizes the degenerate parameter space using MCMC, yielding more accurate uncertainties (Drew & Casey 2022). Our results and discussion do not change if we adopt the CIGALE estimates on dust parameters.

3.1. Dust Mass

We estimate the total dust mass in AzTECC71 following the procedure outlined in Kirkpatrick et al. (2017) using:

$$M_{\rm dust} = \frac{S_\nu D_L^2}{\kappa_\nu B_\nu(T_{\rm dust})}, \quad (1)$$

where D_L is the luminosity distance at $z = 5.7$, S_ν is the flux density, B_ν is the Planck equation, and κ_ν is the dust opacity from Weingartner & Draine (2001) assuming MW-like dust and $R_V = 3.1$. As explained in Kirkpatrick et al. (2017), the variation in κ_ν along the Rayleigh–Jeans (RJ) tail of the cold dust emission is <10% between the MW, SMC, and LMC opacity models. This is lower than the measurement and model uncertainty limiting our dust mass calculation. We fix the cold dust temperature in our calculations to $T_{\rm dust} = 25$ K because this is more representative of the mass-weighted dust temperature rather than the light-weighted dust temperature we get from the SED fits (Scoville et al. 2016).

We use the MCIRSED best-fit SED flux and uncertainty at $\lambda_{\rm obs} = 2$ mm to calculate a dust mass using Equation (1). AzTECC71 is in ExMORA (A. Long et al. 2023, in preparation), a blind 2 mm mosaic that reaches an rms of 60 μJy beam^{-1}. ExMORA lies within the COSMOS-Web footprint and expands the total area of the 2 mm 184 arcmin^2 MORA survey by a factor of ∼4 (Casey et al. 2021). At $z = 5.7$, the 2 mm data probe the RJ tail of cold dust emission ($\lambda_{\rm rest} \sim 300$ μm). This regime is well-suited to measuring the total dust mass because (1) the temperature dependence along the RJ tail is linear, and (2) the emission is optically thin at long wavelengths in the submillimeter (Scoville et al. 2014). While there might be variation in the dust opacity law at $z > 4$ (e.g., Cooper et al. 2022), Faisst et al. (2020a) find optically thin dust at $\lambda_{\rm rest} > 200$ μm in $z \sim 5.5$ galaxies based on three ALMA bands sampling beyond the peak of the IR SED in UV-selected main-sequence galaxies.

We then calculate $M_{\rm dust}$ by randomly sampling the range in $S_{\nu,2\rm mm}$ from the MCIRSED fit (see purple shaded region in Figure 4), as well as the posteriors for β. We repeat this process 1000 times and take the most frequent $M_{\rm dust}$ as our estimate. We report upper and lower uncertainties from the 16th and 84th percentiles of the distribution. From these calculations we estimate the dust mass in AzTECC71 to be $\log M_{\rm dust}/M_\odot = 8.1^{+0.3}_{-0.3}$. If we

Table 2
AzTECC71 Derived Properties

Band	Parameter	Measurement	Units
All ✓	$z_{\rm phot}$	$5.7^{+0.8}_{-0.7}$	⋯
FIR	$z_{\rm phot}$	$4.2^{+3.1}_{-1.6}$	⋯
All	$p(z > 5)$	0.79	⋯
All	$p(z > 4)$	0.99	⋯
All	$p(z < 3)$	3×10^{-5}	⋯
FIR	$p(z > 4)$	0.74	⋯
Assuming $z = 5.7$			
All	M_*	4 ± 2	$10^{10}\,M_\odot$
All ✓	SFR	800^{+400}_{-360}	$M_\odot$ yr^{-1}
All	$L_{\rm IR}$	4 ± 3	$10^{12}\,L_\odot$
All	$T_{\rm dust}$	50^{+20}_{-20}	K
All	A_V	5 ± 1	mag
FIR ✓	$L_{\rm IR}$	6^{+4}_{-3}	$10^{12}\,L_\odot$
FIR	$\lambda_{\rm peak}$	83^{+25}_{-21}	μm
FIR ✓	$T_{\rm dust}$	60^{+22}_{-19}	K
FIR	$\log M_{\rm dust}$	$8.1^{+0.3}_{-0.3}$	$M_\odot$
FIR	$\rm SFR_{IR}$	1000^{+600}_{-500}	$M_\odot$ yr^{-1}
FIR	$\tau_{\rm gas\ depl.}$	12^{+38}_{-8}	Myr
F444W	$n_{\rm sersic}$	0.74 ± 0.02	⋯
F444W	$r_{1/2}$	0.32 ± 0.01	arcsec
B6	$r_{\rm eff}$	<0.44	arcsec
B6	$\Sigma_{\rm IR}$	>1.2	$10^{11}\,L_\odot$ kpc^{-2}

Note. Parameters derived from fits to "All" ("FIR") bands come from CIGALE (MMPz/MCIRCSED). SFR $_{\rm IR}$ is derived from $L_{\rm IR}$ in the FIR fits using $\rm SFR_{IR}/[M_\odot\ yr^{-1}] = 1.8 \times 10^{-10}\,L_{\rm IR}/L_\odot$ (Kennicutt 1998). We indicate our adopted values for physical parameters with a ✓ when estimates are available from both CIGALE and MMPz/MCIRSED.

instead use the ALMA/B6 flux at $\lambda_{\rm obs} = 1250\,\mu$m following the same procedure, we obtain a value consistent within 1σ of $\log M_{\rm dust}/M_\odot = 8.3^{+0.4}_{-0.2}$; however, 1250 μm may or may not be tracing the RJ tail given our photometric redshift uncertainties so we adopt the estimate anchored to the 2 mm upper limit/SED as our fiducial dust mass.[31] AzTECC71's dust mass is close to the total dust mass among $z = 0$ LIRGs, and $\sim$1 dex below the typical dust mass for $z \sim 2$ LIRGs of similar stellar mass to AzTECC71 (Kirkpatrick et al. 2017). Applying this same method to the sample of Faisst et al. (2020a) to eliminate the uncertainty introduced by using different methods to calculate the dust mass, we find a range in dust mass between $\log M_{\rm dust}/M_\odot = 7.6$–$7.8(\pm 0.3)$. Relative to these $z \sim 5.5$ main-sequence galaxies from the UV-selected ALPINE survey (Faisst et al. 2020a), AzTECC71 has a greater dust mass by a factor of $\sim$3 and a higher star formation rate by a factor of $\sim$8 on average. Assuming a gas-to-dust ratio of 100 AzTECC71's depletion timescale ($\tau_{\rm gas\ depl.} \equiv M_{\rm gas}/{\rm SFR}$) is $\sim$15 Myr and could be between 4 and 50 Myr given the uncertainties. Assuming no further gas accretion, AzTECC71 would deplete 99% of its gas reservoir in $\sim$50–100 Myr and could therefore plausibly evolve into the emergent population of quiescent galaxies at $z \sim 4$–5 (e.g., Merlin et al. 2019; Santini et al. 2019; Shahidi et al. 2020; Long et al. 2023).

4. Results and Discussion

4.1. Comparison to High-redshift Samples of Dusty, Star-forming Galaxies

AzTECC71 stands out from high-redshift dusty, star-forming galaxies for its relatively faint optical and NIR photometry. This galaxy is therefore representative of "optical/NIR dark" (hereafter OIR-dark) samples selected in the FIR/submillimeter (da Cunha et al. 2015; Williams et al. 2019; Manning et al. 2022). Approximately 30% of submillimeter-selected galaxies have always been unconstrained in the optical/NIR (Wardlow et al. 2011; Simpson et al. 2014; Casey et al. 2014; Zavala et al. 2018). We now discuss AzTECC71's properties relative to the larger population of submillimeter-selected sources and the subset that are faint/undetected in the optical. We also compare against UV/optical/NIR selected sources that may also have $z > 4$ and high dust content as implied by their optical attenuation or dust continuum follow-up.

AzTECC71 exhibits stellar and dust properties found among larger submillimeter-selected samples. Its SFR, stellar mass, A_V, and dust mass are within the range spanned by 850 μm selected SMG samples from ALESS (da Cunha et al. 2015; Miettinen et al. 2017; Dudzevičiūtė et al. 2020), all of which have redshift distributions peaking at $z \sim 2$–3 with tails extending up to $z \sim 5$–6. Notably AzTECC71's specific star formation rate (sSFR $\equiv$ SFR/M_*) is $25 \pm 17\,{\rm Gyr}^{-1}$, larger than that of galaxies from these samples on average, primarily because of AzTECC71's lower stellar mass than the average of $\sim 10^{11}\,M_\odot$ for $z < 4$ SMGs. AzTECC71 also has a lower dust mass than these SMG samples by 0.5–1 dex. This is all consistent with AzTECC71's higher redshift and having less time to assemble its stars and accrue a dust reservoir.

A number of works have investigated the optically undetected/faint subset of SMGs. AzTECC71 is generally consistent with these samples as well. Smail et al. (2021) analyzed the largest sample selected to have $K_{\rm AB} > 23.5$ from 850 μm selected SMGs. They found on-average higher redshifts ($\langle z \rangle \sim 3.4$), as well as more extreme optical attenuation ($A_V \sim 5$) compared to the parent sample of SMGs, which is to be expected by the faint NIR selection of this subset. Manning et al. (2022) reported two 2 mm selected optically dark $z > 3$ dusty galaxies, both of which are similar to AzTECC71 in terms of the stellar mass and $L_{\rm IR}$, and closer in redshift to AzTECC71 than $K_{\rm AB}$-selected SMGs likely owing to the 2 mm selection function preferring $z > 3$ (Casey et al. 2018; Cooper et al. 2022). Indeed, 2 mm and longer wavelength selection of submillimeter-bright sources preferentially find $z > 5$ OIR-faint/dark galaxies, as is the case for MAMBO-9 (Casey et al. 2019; Jin et al. 2019) and COS-3 mm-1 (Williams et al. 2019; see Figure 4). These sources are good comparisons to the optically faint 850 μm selected HDF850.1 after accounting for magnification (Serjeant & Marchetti 2014). The body of literature on JWST-faint selected SMGs is still in its infancy so the NIRCam selection of objects like AzTECC71 is uncertain. Zavala et al. (2023) identify CEERS-DSFG1, an optically dark galaxy with a 2.25 mJy SCUBA-2 850 μm flux at $z = 4.91$ (Arrabal Haro et al. 2023) detected only in F277W and longer filters like AzTECC71. CEERS-DSFG1 is less extreme with $\log L_{\rm IR}/L_\odot \sim 12$ (Zavala et al. 2023), highlighting the potential population diversity within optically dark, FIR-bright sources that JWST will uncover. In general, the red F277W-F444W and F150 dropout properties of AzTECC71 and objects like CEERS-DSFG1 seem to select galaxies at $z > 4$ that are also highly attenuated. The higher redshifts relative to $K_{\rm AB}$-faint and/or HST-faint/dark selection methods are likely because of the great improvement in sensitivity of NIRCam in the NIR over previous ground/space-based limits.

Prior to JWST AzTECC71 would not have been identified by rest-frame optical/NIR methods for selecting high-z dusty galaxies for lack of a detection shortward of the submillimeter. Unsurprisingly then AzTECC71 is dustier than UV-selected (prior to JWST) $z > 4$ star-forming galaxies with FIR detections from ALMA-REBELS (Inami et al. 2022) and ALPINE (Béthermin et al. 2020; Faisst et al. 2020b), with a larger dust mass by a factor of $\sim$3. This is consistent with AzTECC71 being a $z \sim 5$ starburst possibly fueled by a large gas reservoir whereas the UV-selection of ALPINE and ALMA-REBELS selects predominantly main-sequence galaxies. In Figure 4 we compare AzTECC71 against the average SED of $z > 3$ HST and Spitzer $H - [4.5]$ selected objects from Wang et al. (2016)—"HIEROs." While thought to include a significant fraction of $z > 3$ dusty star-forming galaxies, such HIEROs are $\sim$2 dex brighter in the NIR than AzTECC71, as expected by the selection bias in this wavelength regime. HIEROs are much fainter in the FIR/submillimeter than AzTECC71 if we normalize them to AzTECC71's redshift and IRAC(4.5 μm) flux, which suggests that AzTECC71 is not drawn from this optically faint galaxy population selected in the optical that falls between $3 < z < 6$ (Wang et al. 2016). In fact, AzTECC71 is even missed by H-dropout selection of optically dark IRAC sources despite having comparable $\sim$850 μm flux densities (Wang et al. 2019)

[31] We note that our derived dust mass decreases by a factor of 0.7 dex $\propto (T_{d,{\rm light}}/T_{d,{\rm mass}})^2$ if we were to instead use the light-weighted dust temperature $T_{\rm dust} \sim 60$ K. We reiterate that the light-weighted dust temperature is biased toward the warmest regions whereas a mass-weighted temperature is more representative of the total dust mass and should vary little over the galaxy as the 1/6 power of the average radiation field density.

because of it is higher redshift and extreme optical attenuation. This highlights the importance of both near- and FIR/submillimeter-selected samples of high-z dusty, star-forming galaxies for completeness.

4.2. Morphology

Spatially resolved optical and infrared emission in high-redshift, dusty galaxies commonly show offsets from one another on the order of 0.″2–0.″6 (e.g., Elbaz et al. 2018; Franco et al. 2018). This can arise from differential dust attenuation across the galaxy, in particular due to clumpy dust distributions (e.g., Seibert et al. 2005; Cortese et al. 2006; Boquien et al. 2009; Muñoz-Mateos et al. 2009; Faisst et al. 2017). Interestingly, the NIR and 1250 μm continuum in AzTECC71 are remarkably coincident. Both the ALMA Band 6 peak and centroid agree with the F444W centroid within 0.″1 (Figure 2). While AzTECC71 is not spatially resolved by ALMA, the effective radius at 1250 μm must be below 0.″44 (<2.6 kpc at $z = 5.7$), which could cover a large fraction of the stellar light given AzTECC71's half-light radius of 0.″32 at 4.44 μm. AzTECC71 has a $r_{1/2\,\mathrm{F444W}}$ consistent with the range of NIR sizes in $z \sim 4$ $JH-$blue HIEROs from Wang et al. (2016), and smaller than the average $H-$band sizes of $z \sim 2$ SMGs from Swinbank et al. (2010) by ∼40%. A high dust-covering fraction could help explain the high $A_V = 5$ needed to fit the rest-frame optical photometry, but there is also evidence from the RGB image (Figure 2) that the galaxy is bluer toward the outskirts. Indeed the F277W emission is clumpy and brighter away from the F444W and ALMA centroids, which suggests strong central attenuation. Spatially resolved FIR observations are needed to fully test the resolved impact of dust on reddening across this galaxy only 1.2 Gyr after the Big Bang. Nevertheless, AzTECC71 likely hosts a very dusty nuclear starburst.

Given the size constraint from the ALMA Band 6 continuum detection, AzTECC71 must have a high IR surface density ($\Sigma_{\mathrm{IR}} \equiv 0.5 L_{\mathrm{IR}}/\pi r_{\mathrm{eff}}^2$) above $10^{11}\,L_\odot\,\mathrm{kpc}^{-2}$. This is consistent with the high IR surface densities observed for dusty, star-forming galaxies locally and at high-redshift (Díaz-Santos et al. 2017; Fujimoto et al. 2017; Simpson et al. 2017; Jin et al. 2022b), and could help explain the warm dust temperature preferred by our FIR modeling as a compact starburst heats dust to high temperatures, more so if the gas-phase metallicity is low (Rémy-Ruyer et al. 2014; Sommovigo et al. 2022). Using radiative transfer modeling Hirashita & Chiang (2022) argue that dust temperatures of ∼40 K and above could possibly be explained with lower dust-to-gas ratios. Temperatures below 40 K are not preferred by our FIR SED modeling (Figure 7), but coverage over the FIR SED peak is needed to robustly measure T_{dust} given degenerative solutions with both L_{IR} and β. Taking these measurements at face value suggests a slightly higher dust temperature for this dust-obscured galaxy, which could be related to lower dust-to-gas ratios, metallicity, and/or a heavily obscured AGN, which we cannot rule out for lack of data in the rest-frame mid-IR (e.g., Kirkpatrick et al. 2015; McKinney et al. 2021).

4.3. Implications for High-z Star-forming Galaxy Populations

The incidence of objects like AzTECC71 in upcoming JWST surveys will provide a key test on obscured star formation and the production of dust in the early Universe. First and foremost, AzTECC71 is too faint to have been detected in optical/NIR surveys of the COSMOS field prior to JWST, suggesting that this galaxy could represent a missing component in the total star formation rate density at $z > 5$ estimated from optical/NIR selected samples (see also Algera et al. 2023). The incidence of large dust reservoirs at such early times and their role in attenuating stellar light could have profound implications on early galaxy formation.[32] In particular, dust may be assembled efficiently by supernovae (SNe) in the first 0.5–1 Gyr of galaxy formation compared to more prominent channels active at low $-z$ (Gall et al. 2011; Popping et al. 2017). If so, the optical attenuation laws are likely very different from prescriptions calibrated in the Milky Way owing to changes in the dust grain size distribution in SNe versus AGB-star/molecular cloud production scenarios (Mancini et al. 2016; Graziani et al. 2020). Therefore, large dust masses at $z > 5$ challenge dust production models with implications for all physical properties derived in the rest-frame optical/NIR requiring dust corrections.

AzTECC71's NIR colors are not unique, alluding to many more massive and dusty galaxies at $z > 4$. We show in Figure 8 the F444W/F277W color–magnitude space occupied by galaxies in the COSMOS-Web 2023 January coverage (Casey et al. 2023). Starting with SCUBA-2 detections and validating counterparts with VLA 3 GHz imaging and then Spitzer MIPS and IRAC counterparts, the bulk of the SMGs within the COSMOS-Web footprint are bright in Spitzer and have F444W ∼20–22 magnitudes. However, radio-selected SMGs are biased toward lower redshifts ($z < 4$) owing to positive k-correction at 3 GHz (e.g., Novak et al. 2017; Talia et al. 2021). AzTECC71 is redder than radio-selected SMGs fainter in F444W as well as known $4 < z_{\mathrm{phot}} < 6$ massive galaxies from COSMOS2020 (Weaver et al. 2022), consistent with its higher redshift. We also compare against more typical $z \sim 2$–4 SMGs from ALESS (da Cunha et al. 2015). We redshift the average ALESS SEDs binned by A_V to $z \sim 5$–6. These SED tracks are consistent with AzTECC71's F2777W-F444W color when $A_V > 3$ and $z > 4$, suggesting that some fraction of sources with F277W-F444W > 0.5 and F444W > 24 could be similar $z > 5$ dusty, star-forming galaxies.

There are 627 objects in the COSMOS-Web area analyzed in this work with F277W−F444W > 0.5. Of these, 80 (13%) drop out of the F150W filter and have F444W > 26 magnitude, 15 (2%) are SMGs with a radio counterpart, and we infer 21 (3%) are $4 < z < 6$ and $M_* > 10^{10}\,M_\odot$ with photo-z's from COSMOS2020. 300 (48%) of these galaxies have no counterpart from COSMOS2020 within 1″. Their division between a broader OIR-faint galaxy population and an OIR-faint FIR-bright (e.g., $S_{\nu,850\,\mu\mathrm{m}} \gtrsim 1$ mJy) one could change the inferred dust-obscured star formation density at $z \sim 4$–6. Barrufet et al. (2023) argue that HST-dark JWST-detected galaxies heavily obscured in the optical and with $\log M_*/M_\odot < 10.5$ might dominate over the more massive SMGs at $z > 5$, which could push the dust-obscured star formation rate density to larger values than previously measured from bright 2 mm sources (Casey et al. 2021; Zavala et al. 2021). We find four more objects like AzTECC71 with ALMA counterparts to SCUBA-2 detections in the COSMOS-Web 2023 January footprint. These sources also drop out of the F150W filter, have $\log M_*/M_\odot > 10$ and SFR $> 100\,M_\odot\,\mathrm{yr}^{-1}$, and are likely to lie at $z_{\mathrm{phot}} > 4$ by virtue of bright FIR emission combined with F277W−F444W >0.5 (S. Manning et al. 2023, in preparation). If

[32] See da Cunha (2023) for a concise review.

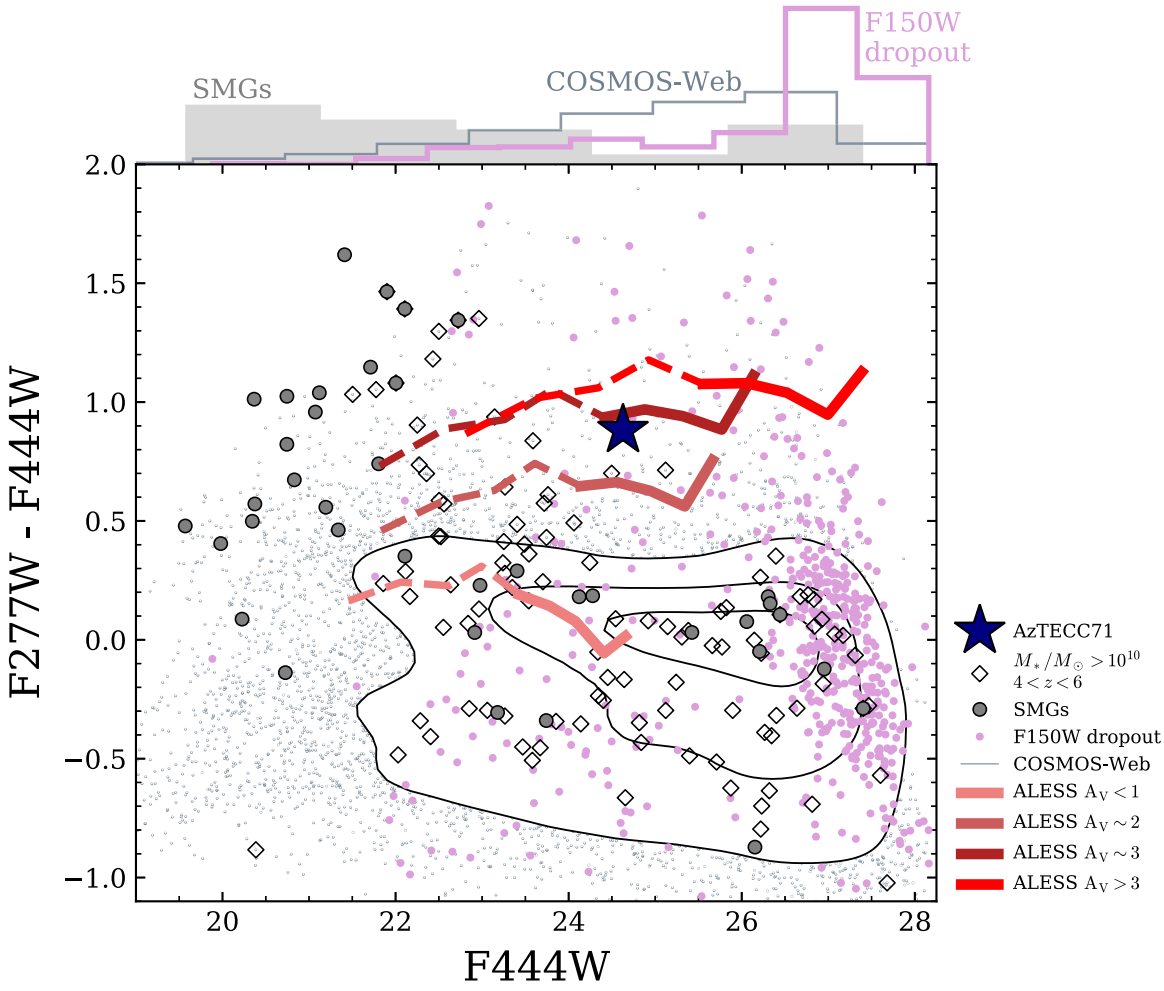

Figure 8. F444W/F277W color–magnitude diagram for galaxies in COSMOS-Web. We show every galaxy over the 77 arcmin^2 area in the background, with contours drawn at the 16th, 50th, and 84th percentiles. From within that sample, we highlight F444W sources that drop out of the F150W filter (purple circles), and $4 < z < 6$, $M_*/M_\odot > 10^{10}$ galaxies with counterparts in COSMOS2020 (diamonds; Weaver et al. 2022). SMGs with 3 GHz counterparts are shown with dark gray circles. Red tracks correspond to redshifted empirical SEDs between $z = 2$–4 (dashed) and $z = 4$–6 (solid) from the ALESS sample (da Cunha et al. 2015) at progressively higher A_V. We normalize the ALESS tracks such that the F444W flux is approximately that of the averaged optically faint ALESS SEDs for their mean redshift: ∼2 nJy for $\langle z \rangle^{ALESS}_{OIR-faint} = 3.7$ (da Cunha et al. 2015). AzTECC71 (black star) is among the reddest population of galaxies found in the first six pointings of COSMOS-Web, is redder than known $4 < z_{phot} < 6$ massive galaxies from COSMOS2020, and is brighter in F444W than most objects that drop out of F150W. AzTECC71 is also the faintest F444W source with F277W-F444W >0.2 and an FIR counterpart confirmed with an ALMA or VLA detection.

we assume that all of these sources have $z > 4$ and given the current area of COSMOS-Web's footprint (77 arcmin^2), we estimate a volume density of $4 < z < 6$ dusty, star-forming galaxies with $\log L_{IR}/L_\odot > 11$ of $\log n/\mathrm{Mpc}^{-3} \sim 5 \pm \mathbf{0.2}$. This is high relative to the median reported in the literature ($10^{-5.5}$ Mpc^{-3}, as compiled by Long et al. 2023), which may require revised estimates on the depletion/quenching timescale in the first ∼Gyr of galaxy formation and a higher incidence of dust-obscured star formation in general at this epoch. However, a volume density calculated over both a larger sample and area is needed to fully establish the incidence of objects like AzTECC71.

Presently, the disparity in reported volume densities for massive and dusty sources is largely due to different survey areas and wavelengths (Long et al. 2023). The full 0.54 deg^2 COSMOS-Web survey field will be key in overcoming this global uncertainty by covering sufficient area to minimize the effects of cosmic variance (Casey et al. 2023). Notably this is not achieved in the 2023 January data, which cover 77.76 arcmin^2. Following the analytical approach outlined in Moster et al. (2011), we estimate the cosmic variance (σ_v^2) of $\log M_*/M_\odot \sim 10.5$ sources between $4 < z < 6$ in the 2023 January COSMOS-Web footprint to be $\sigma_v^2 = 0.5$. Quantities derived from the survey area, such as the volume density, are less prone to cosmic variance when $\sigma_v^2 < 0.15$, as will be the case for the 0.54 deg^2 COSMOS-Web mosaic for which we estimate $\sigma_v^2 < 0.05$ over the same mass and redshift range. Reproducing the selection function described in this work over all of COSMOS-Web will place robust constraints on the number density of massive, obscured galaxies at $z > 4$.

5. Summary and Conclusion

We report the JWST/NIRCam detection from the COSMOS-Web survey of AzTECC71, a known submillimeter source with no previous detection below 850 μm. We identify counterparts in NIRCam/F277W and F444W using ALMA Band 6 imaging to localize the submillimeter emission. AzTECC71 is not detected in the COSMOS-Web F115W and F150W images, or in other ground- or space-based imaging below 2.7 μm. Based on multiwavelength SED modeling, AzTECC71 is a massive ($\log M_*/M_\odot = 10.6$) and

IR-luminous ($\log L_{\rm IR}/L_{\odot} = 12.75$) galaxy with a high (>99%) probability of being at $z > 4$ and $z_{\rm phot} = 5.7$.

AzTECC71 is broadly similar with respect to stellar properties and FIR flux densities to known optically dark/faint dusty, star-forming galaxies (Williams et al. 2019; Smail et al. 2021; Talia et al. 2021; Manning et al. 2022). This object is the faintest confirmed F444W counterpart to submillimeter galaxies in COSMOS-Web to date with $S/N_{850\mu m} > 4$ and F277W-F444W > 0.25, and a member to a larger sample of high-redshift dusty, star-forming galaxies with no prior optical/NIR counterpart (S. Manning et al. 2023, in preparation). If ALMA-confirmed submillimeter sources that drop out of F150W in COSMOS-Web collectively fall at $z > 4$ as is the case for AzTECC71, then the number counts of luminous, infrared galaxies at $4 < z < 6$ would be 0.5 dex higher than the median reported in the literature (Long et al. 2023). This could require revised estimates on the $z > 4$ IR star formation rate density, as well as for the quenching timescale of dusty, star-forming galaxies at this epoch.

The hunt for and characterization of optically faint FIR-bright galaxies stands on a precipice. The combination of JWST, ALMA, and VLA has significantly improved our capacity to find counterparts to bright FIR/submillimeter sources and characterize the stellar populations in high-redshift ($z > 4$) dusty, star-forming galaxies. In parallel, the upcoming generation of deep imaging surveys with JWST is finding very faint optical/NIR sources that plausibly occupy the LIRG regime at $z > 4$–6 but lack IR coverage necessary to robustly confirm or deny a high dust-obscured star formation rate. At this epoch the incidence of dusty star-forming galaxies remains unconstrained owing to limiting sensitivities of ground-based FIR facilities that struggle to survey below the ULIRG limit at $z > 4$, though there is some evidence for more obscured star formation than previously thought at this epoch (Wang et al. 2016; Gruppioni et al. 2020; Talia et al. 2021; Barrufet et al. 2023; Pérez-González et al. 2023; Rodighiero et al. 2023). Moreover, the "optically faint" classification is becoming a confusing identifier as the population diversity of objects discovered for the first time in the optical by JWST grows. Upcoming instruments such as TolTEC on the Large Millimeter Telescope will push to deeper $L_{\rm IR}$ limits with ~5″ resolution at 1.1 mm, enabling better counterpart matching between large optical/NIR and FIR surveys. With these state-of-the-art data sets, OIR-faint/dark galaxies should distinguish between FIR-bright or FIR-faint populations in classification schemes where possible. Even then, a cold FIR space telescope with a large aperture of sufficient spectroscopic sensitivity to disentangle confused sources along the frequency axis is needed fully uncover the very distant IR Universe.

Acknowledgments

We thank the referee for their constructive comments, which helped contextualize the manuscript with other works and clarify the message. J.M. would like to thank C. Williams for making the SED of COS-3 mm-1 readily available, and the NRAO/ALMA Helpdesk team for making archival data easy to access. This work is based [in part] on observations made with the NASA/ESA/CSA JWST. The data were obtained from the Mikulski Archive for Space Telescopes at the Space Telescope Science Institute, which is operated by the Association of Universities for Research in Astronomy, Inc., under NASA contract NAS 5-03127 for JWST. These observations are associated with program ID 1727. Support for program 1727 was provided by NASA through a grant from the Space Telescope Science Institute, which is operated by the Association of Universities for Research in Astronomy, Inc., under NASA contract NAS 5-03127. This paper makes use of the following ALMA data: ADS/JAO.ALMA:2013.1.00118.S. ALMA is a partnership of ESO (representing its member states), NSF (USA), and NINS (Japan), together with NRC (Canada), MOST and ASIAA (Taiwan), and KASI (Republic of Korea), in cooperation with the Republic of Chile. The Joint ALMA Observatory is operated by ESO, AUI/NRAO, and NAOJ. The National Radio Astronomy Observatory is a facility of the National Science Foundation operated under a cooperative agreement by Associated Universities, Inc. This work used the CANDIDE computer system at the IAP supported by grants from the PNCG, CNES, and the DIM-ACAV and maintained by S. Rouberol.

ORCID iDs

Jed McKinney https://orcid.org/0000-0002-6149-8178
Sinclaire M. Manning https://orcid.org/0000-0003-0415-0121
Olivia R. Cooper https://orcid.org/0000-0003-3881-1397
Arianna S. Long https://orcid.org/0000-0002-7530-8857
Hollis Akins https://orcid.org/0000-0003-3596-8794
Caitlin M. Casey https://orcid.org/0000-0002-0930-6466
Andreas L. Faisst https://orcid.org/0000-0002-9382-9832
Maximilien Franco https://orcid.org/0000-0002-3560-8599
Christopher C. Hayward https://orcid.org/0000-0003-4073-3236
Erini Lambrides https://orcid.org/0000-0003-3216-7190
Georgios Magdis https://orcid.org/0000-0002-4872-2294
Katherine E. Whitaker https://orcid.org/0000-0001-7160-3632
Min Yun https://orcid.org/0000-0001-7095-7543
Jaclyn B. Champagne https://orcid.org/0000-0002-6184-9097
Nicole E. Drakos https://orcid.org/0000-0003-4761-2197
Fabrizio Gentile https://orcid.org/0000-0002-8008-9871
Steven Gillman https://orcid.org/0000-0001-9885-4589
Ghassem Gozaliasl https://orcid.org/0000-0002-0236-919X
Olivier Ilbert https://orcid.org/0000-0002-7303-4397
Shuowen Jin https://orcid.org/0000-0002-8412-7951
Anton M. Koekemoer https://orcid.org/0000-0002-6610-2048
Vasily Kokorev https://orcid.org/0000-0002-5588-9156
Daizhong Liu https://orcid.org/0000-0001-9773-7479
R. Michael Rich https://orcid.org/0000-0003-0427-8387
Brant E. Robertson https://orcid.org/0000-0002-4271-0364
Francesco Valentino https://orcid.org/0000-0001-6477-4011
John R. Weaver https://orcid.org/0000-0003-1614-196X
Jorge A. Zavala https://orcid.org/0000-0002-7051-1100
Natalie Allen https://orcid.org/0000-0001-9610-7950
Jeyhan S. Kartaltepe https://orcid.org/0000-0001-9187-3605
Henry Joy McCracken https://orcid.org/0000-0002-9489-7765
Louise Paquereau https://orcid.org/0000-0003-2397-0360
Jason Rhodes https://orcid.org/0000-0002-4485-8549
Marko Shuntov https://orcid.org/0000-0002-7087-0701
Sune Toft https://orcid.org/0000-0003-3631-7176

References

Algera, H. S. B., Inami, H., Oesch, P. A., et al. 2023, MNRAS, 518, 6142
Aretxaga, I., Wilson, G. W., Aguilar, E., et al. 2011, MNRAS, 415, 3831
Arrabal Haro, P., Dickinson, M., Finkelstein, S. L., et al. 2023, arXiv:2303.15431

Bagley, M. B., Finkelstein, S. L., Koekemoer, A. M., et al. 2023, ApJL, 946, L12
Barrufet, L., Oesch, P. A., Weibel, A., et al. 2023, MNRAS, 522, 449
Bertoldi, F., Carilli, C., Aravena, M., et al. 2007, ApJS, 172, 132
Béthermin, M., Fudamoto, Y., Ginolfi, M., et al. 2020, A&A, 643, A2
Boquien, M., Burgarella, D., Roehlly, Y., et al. 2019, A&A, 622, A103
Boquien, M., Calzetti, D., Kennicutt, R., et al. 2009, ApJ, 706, 553
Brisbin, D., Miettinen, O., Aravena, M., et al. 2017, A&A, 608, A15
Casey, C. M. 2012, MNRAS, 425, 3094
Casey, C. M. 2020, ApJ, 900, 68
Casey, C. M., Chen, C.-C., Cowie, L. L., et al. 2013, MNRAS, 436, 1919
Casey, C. M., Kartaltepe, J. S., Drakos, N. E., et al. 2023, ApJ, 954, 31
Casey, C. M., Narayanan, D., & Cooray, A. 2014, PhR, 541, 45
Casey, C. M., Zavala, J. A., Aravena, M., et al. 2019, ApJ, 887, 55
Casey, C. M., Zavala, J. A., Manning, S. M., et al. 2021, ApJ, 923, 215
Casey, C. M., Zavala, J. A., Spilker, J., et al. 2018, ApJ, 862, 77
Chabrier, G. 2003, PASP, 115, 763
Chen, C.-C., Cowie, L. L., Barger, A. J., et al. 2013, ApJ, 776, 131
Cooper, O. R., Casey, C. M., Zavala, J. A., et al. 2022, ApJ, 930, 32
Cortese, L., Boselli, A., Buat, V., et al. 2006, ApJ, 637, 242
Cowie, L. L., Barger, A. J., Wang, W. H., & Williams, J. P. 2009, ApJL, 697, L122
da Cunha, E. 2023, in IAU Symp. 373, Resolving the Rise and Fall of Star Formation in Galaxies, ed. T. Wong & K. Woong-Tae (Cambridge: Cambridge Univ. Press), 215
da Cunha, E., Groves, B., Walter, F., et al. 2013, ApJ, 766, 13
da Cunha, E., Walter, F., Smail, I. R., et al. 2015, ApJ, 806, 110
Danielson, A. L. R., Swinbank, A. M., Smail, I., et al. 2017, ApJ, 840, 78
Delvecchio, I., Daddi, E., Sargent, M. T., et al. 2021, A&A, 647, A123
Díaz-Santos, T., Armus, L., Charmandaris, V., et al. 2017, ApJ, 846, 32
Drew, P. M., & Casey, C. M. 2022, ApJ, 930, 142
Dudzevičiūtė, U., Smail, I., Swinbank, A. M., et al. 2020, MNRAS, 494, 3828
Dunlop, J. S., McLure, R. J., Yamada, T., et al. 2004, MNRAS, 350, 769
Elbaz, D., Leiton, R., Nagar, N., et al. 2018, A&A, 616, A110
Faisst, A. L., Capak, P. L., Yan, L., et al. 2017, ApJ, 847, 21
Faisst, A. L., Fudamoto, Y., Oesch, P. A., et al. 2020a, MNRAS, 498, 4192
Faisst, A. L., Schaerer, D., Lemaux, B. C., et al. 2020b, ApJS, 247, 61
Finkelstein, S. L., Bagley, M. B., Ferguson, H. C., et al. 2023, ApJL, 946, L13
Franco, M., Elbaz, D., Béthermin, M., et al. 2018, A&A, 620, A152
Franco, M., Elbaz, D., Zhou, L., et al. 2020, A&A, 643, A53
Fujimoto, S., Ouchi, M., Shibuya, T., & Nagai, H. 2017, ApJ, 850, 83
Gall, C., Andersen, A. C., & Hjorth, J. 2011, A&A, 528, A13
Geach, J. E., Dunlop, J. S., Halpern, M., et al. 2017, MNRAS, 465, 1789
Graziani, L., Schneider, R., Ginolfi, M., et al. 2020, MNRAS, 494, 1071
Gruppioni, C., Béthermin, M., Loiacono, F., et al. 2020, A&A, 643, A8
Hayward, C. C., Behroozi, P. S., Somerville, R. S., et al. 2013, MNRAS, 434, 2572
Hayward, C. C., Chapman, S. C., Steidel, C. C., et al. 2018, MNRAS, 476, 2278
Hirashita, H., & Chiang, I.-D. 2022, MNRAS, 516, 1612
Hodge, J. A., & da Cunha, E. 2020, RSOS, 7, 200556
Holland, W. S., Bintley, D., Chapin, E. L., et al. 2013, MNRAS, 430, 2513
Hughes, D. H., Serjeant, S., Dunlop, J., et al. 1998, Natur, 394, 241
Inami, H., Algera, H. S. B., Schouws, S., et al. 2022, MNRAS, 515, 3126
Jin, S., Daddi, E., Liu, D., et al. 2018, ApJ, 864, 56
Jin, S., Daddi, E., Magdis, G. E., et al. 2019, ApJ, 887, 144
Jin, S., Daddi, E., Magdis, G. E., et al. 2022a, A&A, 665, A3
Jin, S., Daddi, E., Magdis, G. E., et al. 2022b, A&A, 665, A3
Kato, Y., Matsuda, Y., Iono, D., et al. 2018, PASJ, 70, L6
Kennicutt, R. C. J. 1998, ARA&A, 36, 189
Kirkpatrick, A., Pope, A., Sajina, A., et al. 2015, ApJ, 814, 9
Kirkpatrick, A., Pope, A., Sajina, A., et al. 2017, ApJ, 843, 71
Koekemoer, A. M., Aussel, H., Calzetti, D., et al. 2007, ApJS, 172, 196
Koprowski, M. P., Dunlop, J. S., Michałowski, M. J., et al. 2017, MNRAS, 471, 4155
Koprowski, M. P., Dunlop, J. S., Michałowski, M. J., Cirasuolo, M., & Bowler, R. A. A. 2014, MNRAS, 444, 117
Le Floc'h, E., Aussel, H., Ilbert, O., et al. 2009, ApJ, 703, 222
Lim, C.-F., Wang, W.-H., Smail, I., et al. 2020, ApJ, 889, 80
Liu, D., Daddi, E., Dickinson, M., et al. 2018, ApJ, 853, 172
Long, A. S., Casey, C. M., Lagos, C. D. P., et al. 2023, ApJ, 953, 11
Lutz, D., Poglitsch, A., Altieri, B., et al. 2011, A&A, 532, A90
Madau, P., & Dickinson, M. 2014, ARA&A, 52, 415
Mancini, M., Schneider, R., Graziani, L., et al. 2016, MNRAS, 462, 3130
Manning, S. M., Casey, C. M., Zavala, J. A., et al. 2022, ApJ, 925, 23
Martí-Vidal, I., Vlemmings, W. H. T., Muller, S., & Casey, S. 2014, A&A, 563, A136
McKinney, J., Hayward, C. C., Rosenthal, L. J., et al. 2021, ApJ, 921, 55
Merlin, E., Fortuni, F., Torelli, M., et al. 2019, MNRAS, 490, 3309
Michałowski, M. J., Dunlop, J. S., Koprowski, M. P., et al. 2017, MNRAS, 469, 492
Miettinen, O., Delvecchio, I., Smolčić, V., et al. 2017, A&A, 606, A17
Moster, B. P., Somerville, R. S., Newman, J. A., & Rix, H.-W. 2011, ApJ, 731, 113
Muñoz-Mateos, J. C., Gil de Paz, A., Boissier, S., et al. 2009, ApJ, 701, 1965
Murphy, E. J., Chary, R. R., Dickinson, M., et al. 2011, ApJ, 732, 126
Novak, M., Smolčić, V., Delhaize, J., et al. 2017, A&A, 602, A5
Oliver, S. J., Bock, J., Altieri, B., et al. 2012, MNRAS, 424, 1614
Pérez-González, P. G., Barro, G., Annunziatella, M., et al. 2023, ApJL, 946, L16
Popping, G., Somerville, R. S., & Galametz, M. 2017, MNRAS, 471, 3152
Rémy-Ruyer, A., Madden, S. C., Galliano, F., et al. 2014, A&A, 563, A31
Rodighiero, G., Bisigello, L., Iani, E., et al. 2023, MNRAS, 518, L19
Santini, P., Merlin, E., Fontana, A., et al. 2019, MNRAS, 486, 560
Scoville, N., Aussel, H., Brusa, M., et al. 2007, ApJS, 172, 1
Scoville, N., Aussel, H., Sheth, K., et al. 2014, ApJ, 783, 84
Scoville, N., Sheth, K., Aussel, H., et al. 2016, ApJ, 820, 83
Seibert, M., Martin, D. C., Heckman, T. M., et al. 2005, ApJL, 619, L55
Serjeant, S., & Marchetti, L. 2014, MNRAS, 443, 3118
Shahidi, A., Mobasher, B., Nayyeri, H., et al. 2020, ApJ, 897, 44
Shu, X., Yang, L., Liu, D., et al. 2022, ApJ, 926, 155
Simpson, J. M., Smail, I., Swinbank, A. M., et al. 2015, ApJ, 807, 128
Simpson, J. M., Smail, I., Swinbank, A. M., et al. 2017, ApJ, 839, 58
Simpson, J. M., Smail, I., Swinbank, A. M., et al. 2019, ApJ, 880, 43
Simpson, J. M., Swinbank, A. M., Smail, I., et al. 2014, ApJ, 788, 125
Smail, I., Dudzevičiūtė, U., Stach, S. M., et al. 2021, MNRAS, 502, 3426
Smolčić, V., Novak, M., Bondi, M., et al. 2017, A&A, 602, A1
Sommovigo, L., Ferrara, A., Pallottini, A., et al. 2022, MNRAS, 513, 3122
Swinbank, A. M., Smail, I., Chapman, S. C., et al. 2010, MNRAS, 405, 234
Talia, M., Cimatti, A., Giulietti, M., et al. 2021, ApJ, 909, 23
U, V., Sanders, D. B., Mazzarella, J. M., et al. 2012, ApJS, 203, 9
Walter, F., Decarli, R., Carilli, C., et al. 2012, Natur, 486, 233
Wang, T., Elbaz, D., Schreiber, C., et al. 2016, ApJ, 816, 84
Wang, T., Schreiber, C., Elbaz, D., et al. 2019, Natur, 572, 211
Wardlow, J. L., Smail, I., Coppin, K. E. K., et al. 2011, MNRAS, 415, 1479
Weaver, J. R., Kauffmann, O. B., Ilbert, O., et al. 2022, ApJS, 258, 11
Weingartner, J. C., & Draine, B. T. 2001, ApJ, 548, 296
Williams, C. C., Labbe, I., Spilker, J., et al. 2019, ApJ, 884, 154
Zavala, J. A., Aretxaga, I., Dunlop, J. S., et al. 2018, MNRAS, 475, 5585
Zavala, J. A., Buat, V., Casey, C. M., et al. 2023, ApJL, 943, L9
Zavala, J. A., Casey, C. M., Manning, S. M., et al. 2021, ApJ, 909, 165